

AUTOMATIC DETECTION OF MICROANEURYSMS AND HAEMORRHAGES IN FUNDUS IMAGES USING DYNAMIC SHAPE FEATURES

Lama Séoud^{*†}, Timothée Faucon[†], Thomas Hurtut^{*‡}, Jihed Chelbi[†], Farida Cheriet^{*}, J.M. Pierre Langlois^{*}

^{*} Polytechnique Montréal, Canada

[†] Diagnos Inc., Brossard, Canada

[‡] Université Paris Descartes, Paris, France

ABSTRACT

This paper presents a novel approach for automatic detection of microaneurysms and haemorrhages in fundus images. First, it begins with a preprocessing stage for shade correction, contrast enhancement and denoising. Second, all regional minima with sufficient contrast are extracted and considered as candidates. Third, in an image flooding scheme, a new set of dynamic shape features is computed as a function of intensity. Finally, a Random Forest classifies the candidates into lesions and non lesions. A set of 143 fundus images with an average of 2210 pixels in diameter was acquired using different cameras and used for training and testing. The proposed approach achieved a global score over the FROC curve of 0.393, while previous work with images of similar resolution reported a score of 0.233.

Index Terms— Image processing, features extraction, computer aided detection, fundus images.

1. INTRODUCTION

Diabetic retinopathy (DR) is the leading cause of preventable blindness in the working-age population [1]. Early detection, together with appropriate treatment, can help prevent visual impairment. In current diagnostic procedure, a retina specialist analyzes fundus images and visually identifies lesions such as microaneurysms (MA) and haemorrhages (HM). The grade of DR depends mainly on the location, number and type of lesions. With the increasing number of diabetic patients, computer aided detection systems are becoming essential for DR screening and grading [2]. It adds more objectivity and reproducibility to the task and it accelerates the process.

Several methods for red lesions detection are proposed in the literature [3–7]. The most popular approach consists in candidate extraction followed by region classification. Once a candidate is identified, a region growing [4, 5] is performed to find its boundaries. Shape and color features are then computed and used for classification. A major limitation is that the features extracted are consequently highly dependent on the edges found by region growing.

Most of the papers focus mainly on the detection of MAs [3–7]. Because of their regular small circular shape, MAs can be detected or at least enhanced using 2D gaussian match filtering [3, 6] or through local rotation cross-section profile analysis [7]. However, even though MAs are considered as a critical component for DR screening, DR grading requires also the detection of HMs. By using the top-hat filter to remove connected components larger than the structuring element [4, 5], vessels as well as larger HMs are removed and thus missed in subsequent processing.

Several methods proposed in the literature have been built and validated on a common publicly available dataset, the retinopathy online challenge dataset [8]. The reported scores vary between 0.206 and 0.434 [7] depending on the detection algorithm. Unfortunately, the images of this dataset have a resolution much smaller than the one provided by most of the up-to-date retinographs. According to [9], a resolution of 50 pixels per degree of field of view (FOV) is needed to provide diagnostic power comparable to film-based images. Thus, for a 45° FOV, images must have about 2250 pixels on the diameter of the region of interest (ROI), while images of the retinopathy online challenge only have about 540 pixels. Only Lazar et al. [7] considered images with 2200 pixels in diameter for the validation of their detection algorithm, they reported a score of 0.233.

In this paper, a novel approach for the detection of MAs and HMs in high resolution fundus images is proposed and validated. It introduces a novel set of dynamic shape features used for region classification. It is motivated by the fact that the shape of a candidate region depends highly on the intensity threshold for which the region is defined.

2. METHOD

The proposed approach is divided into four steps, each of which will be detailed in the following subsections.

2.1. Image preprocessing

A shade correction is performed to remove variations in the background illumination. A mean filter of size 401×401 is applied to the input image and the result is then subtracted

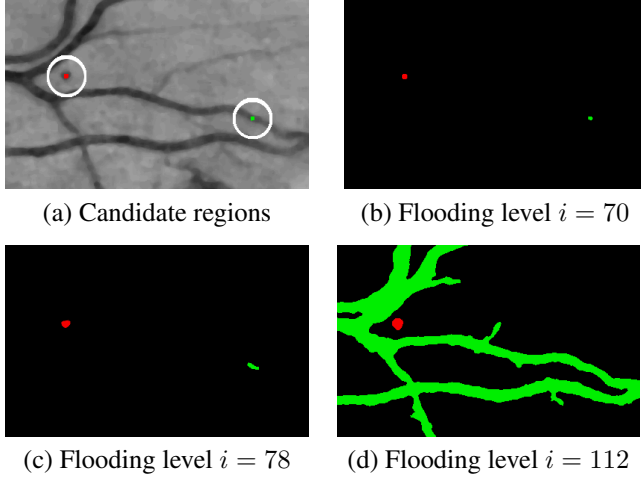


Fig. 1. Morphological flooding of image (a) with 2 candidate regions encircled in white: R_1 (in red) and R_2 (in green). Subfigures (b), (c) and (d) show the resulting catchment basins $C_i^{R_1}$ (in red) and $C_i^{R_2}$ (in green) for $i = 70$, $i = 78$ and $i = 112$, respectively.

from the image. The resulting image is noted I_{sc} . Contrast enhancement is achieved by stretching and clipping the green histogram of I_{sc} on the range $\mu \pm 3\sigma$, where μ and σ are the mean and standard deviation, respectively, of I_{sc} 's green channel. The green channel is considered because of the high contrast it offers around the lesions. Finally, a 7×7 median filter is applied to remove and attenuate the noise resulting from the acquisition and compression steps. The final preprocessed image is noted I_p .

2.2. Candidate extraction

To locate potential red lesions, all regional minima of I_p are identified. A regional minimum is defined as a group of connected pixels with same intensity h , such that all its adjacent pixels have strictly higher intensities [10].

Then, two criteria are applied. First, only minima that are darker than I_p 's mean intensity are considered. Second, only minima with a contrast superior to a threshold K are retained. In a topographic representation of I_p , the contrast of a minimum M is defined as the difference in altitude between M and the highest point of the paths reaching a minimum with lower intensity [11]. The advantage of this definition of contrast is that it is independent on the size and shape of the structure. All remaining minima constitute candidate regions.

2.3. Features extraction

Extracted candidates include red lesions, vessel segments and the fovea. A candidate classification step is required to discriminate between lesions and non lesions. A new set of features is thus proposed in this subsection.

In a topographic representation of I_p , each candidate (a regional minimum) corresponds to a water source, noted R_j .

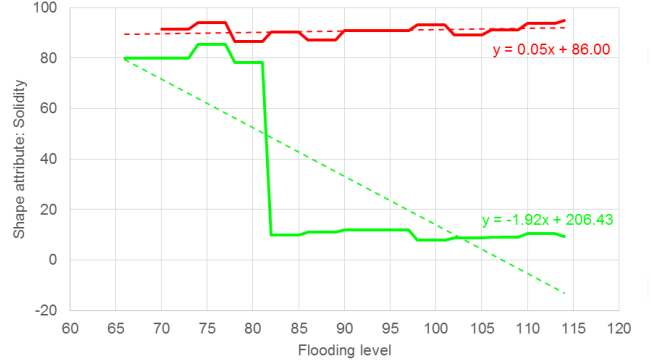


Fig. 2. Solidity curves (in solid lines) for the two candidate regions R_1 (in red) and R_2 (in green) of Fig. 1. The slopes (0.05 and -1.92) and the intercepts (86 and 206.43) of the linear least-square fits (dashed lines) are examples of DSFs.

A morphological flooding, inspired from the watershed algorithm, is applied to I_p starting from the lowest water source and ending when I_p 's mean intensity is reached. At each flooding level i , pixels that are adjacent to a water source R_j and lower than the flooding level i are added to the catchment basin of R_j , noted $C_i^{R_j}$. When two basins merge, they start to share the same pixels and thus the same attributes.

Fig. 1 illustrates three flooding steps with two candidates taken from a single image. The first candidate, noted R_1 and coloured in red, corresponds to a true MA, and the second one, noted R_2 and coloured in green, corresponds to a vessel segment. Throughout the image flooding, R_2 starts as a small compact shape, it then turns into an elongated shape, and finally, it merges with adjacent candidate to form the vessel network. Whereas, R_1 grows more isotropically and remains isolated from other candidates even for higher flooding levels.

At each flooding level i , for each candidate region R_j , 7 shape attributes are computed on the catchment basin $C_i^{R_j}$:

1. Area: number of pixels in $C_i^{R_j}$, divided by the total number of pixels in the ROI.
2. Number of collisions: number of catchment basins merged into $C_i^{R_j}$.
3. Elongation: $1 - W/L$ with W and L the width and length respectively of the bounding box of $C_i^{R_j}$ oriented along its major axis.
4. Excentricity: $\sqrt{(L^2 - W^2)/L^2}$.
5. Circularity: ratio of the area of $C_i^{R_j}$ over its squared perimeter and divided by $1/4\pi$.
6. Rectangularity: ratio of the area of $C_i^{R_j}$ over the area of its bounding box oriented along its major axis.
7. Solidity: ratio of the area of $C_i^{R_j}$ over the area of its convex hull.

For each candidate region, a total of 7 curves are obtained, one for each shape attribute. Each curve corresponds to an

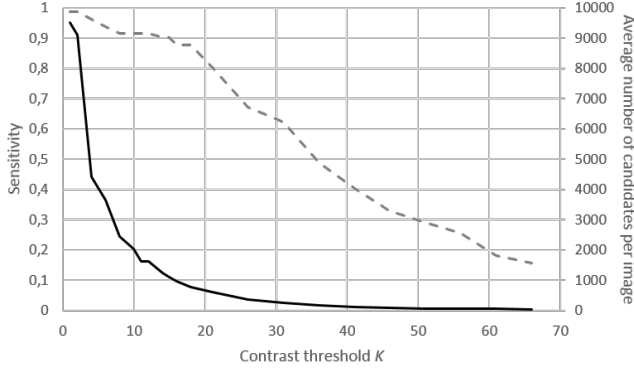


Fig. 3. Sensitivity (dashed line) and average number of candidates per image (solid line) as functions of the contrast threshold K .

attribute’s value as a function of the flooding level i , from the minimum value h_{R_j} to I_p ’s mean intensity. Fig. 2 shows the solidity curves obtained for candidates R_1 (in red) and R_2 (in green) illustrated in Fig. 1. In this example, the image’s mean intensity is 114, and $h_{R_1} = 70$ and $h_{R_2} = 66$.

Each curve is then represented as a vector of 5 dynamic shape features (DSF). The first three are the slope, intercept and root mean squared error of a linear least-square fit of the curve. The last two are the mean and median of the attribute’s values along the curve. In total, $7 \times 5 = 35$ DSFs are computed for each candidate region. Color information is added to the resulting feature vector as 5 separate static features: the RGB values of the regional minima computed on I_{sc} , its intensity h in I_p , and its contrast in I_p , previously calculated according to [11]. In Fig. 2, the linear least-square fits of the solidity curves are represented as dashed lines and the values of two DSFs (the slope and intercept) are shown.

2.4. Classification

To distinguish between lesions and non lesions, we considered a Random Forest (RF) classifier [12]. It is robust to imbalanced training data and incorporates an implicit features selection step. An RF is a combination of T decision trees trained independently using T bootstrap samples from the training set. Each node is split using the best of m features randomly chosen at that node. The output probability of a candidate is given by aggregating the decisions of the T trees. In this study, the RF is made of $T = 500$ trees and $m = \lfloor \sqrt{M} \rfloor = 6$, where $M = 40$ is the number of features.

3. MATERIAL

A dataset of 143 fundus images with 45° FOV and an average of 2210 pixels along the ROI diameter is used. Images were acquired in the context of a tele-medicine project, thus using a large variety of retinographs (different models of Zeiss, Topcon, Canon and Centerview). It is saved in JPEG format, the mean compression rate being 14:1.

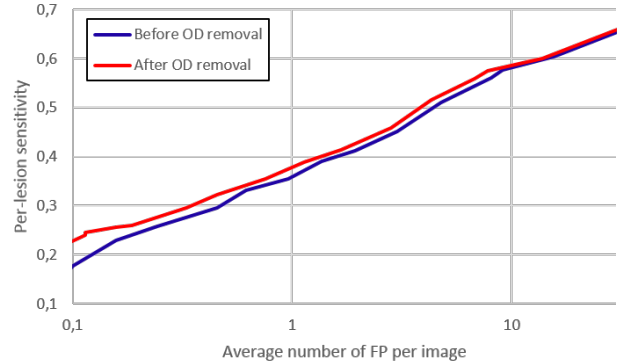


Fig. 4. FROC curves computed on the test images, before and after OD removal.

All red lesions in the dataset were manually segmented without distinction between MAs and HMs. The segmentation was validated by an ophthalmologist. Among the 143 images, 1515 red lesions were found in a total of 56 images, the remaining images being red lesions free. The overall dataset was randomly split into a training set made of 73 images (847 lesions) and a test set made of 70 images (668 lesions).

4. RESULTS AND DISCUSSION

4.1. Performance at the candidate extraction step

Fig. 3 shows the sensitivity and average number of candidates per image for different values of the contrast threshold K . With $K = 15$, the average number of candidates per image is 1115. Over all the manually segmented lesions, only 10% are missed and are not present in the classification step. To the best of our knowledge, only one paper [4] reports the sensitivity at the candidate extraction step. On images with 4 times less pixels in diameter, the sensitivity is 89.8%, for an average of about 300 candidates per image.

4.2. Performance of the RF classifier

To analyze the classification performance of the RF, the ROC curve was computed on the test set and we obtained an area under the curve of 0.932. Considering that only 0.8% of the candidates in the test set correspond to manually segmented lesions, the results demonstrate that the RF classifier efficiently overcomes the high imbalance in our dataset.

4.3. Overall performance

To assess the overall performance of the proposed approach, the FROC curve is computed according to [8]. It is shown in blue on Fig. 4. Qualitative analysis of the results revealed first that both MAs and larger HMs are correctly detected by the proposed algorithm (Fig. 5b), as opposed to most of the methods in the literature which focus solely on detection of MAs. Second, most of the false negatives correspond to lesions directly connected to or very close to vessels (about 5 pixels

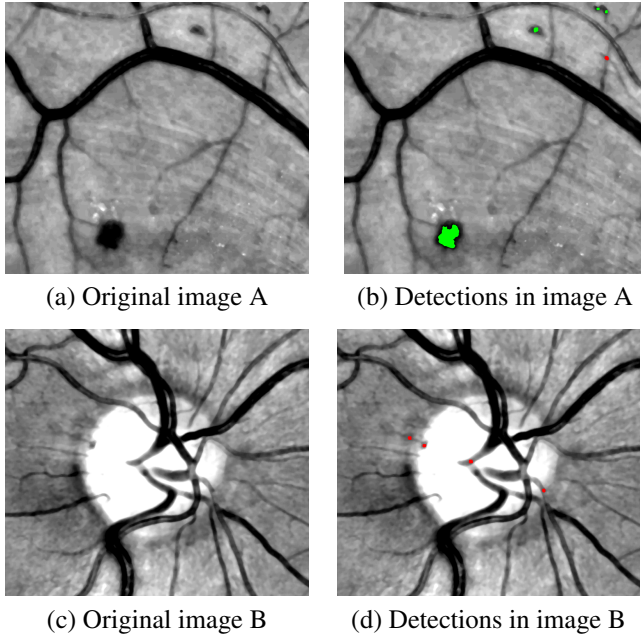


Fig. 5. Examples of true (green) and false (red) positives.

distance). Third, most of the false positives (FP) are located inside the optic disk (OD) (Fig. 5d) and others correspond to vessel crossings (Fig. 5b).

The second FROC curve, shown in red in Fig. 4, is computed after removal of all candidates inside the OD. Automatic detection of the OD is achieved by first, identifying the ROI's subsection with highest variance on a mean filtered version of the image, second, detecting edges in the original image using Canny's filter, and finally, applying Hough's transform for circle detection. The improved results suggest that OD removal should be used as a preprocessing step.

After OD removal, our system's sensitivity is 58% and the average number of FPs per image is 7.8, for a probability threshold of 0.15. The global score of the system, calculated as in [8] over the test set, is 0.367 before OD removal and 0.393 after. Unfortunately, no straightforward comparison with previously published scores can be done since the dataset is different. However, for a rough comparison, the scores obtained on the low resolution images of the retinopathy online challenge vary between 0.206 and 0.434 [7]. The only method [7] that was validated on images with a resolution similar to ours achieved a score of only 0.233 which is lower than ours.

5. CONCLUSION

A novel method for MAs and HMs detection is proposed in this paper. It is developed and validated on images with a resolution similar to the one provided by most state-of-the-art retinographs. The performance of the system is higher than the one proposed in the literature for images of similar reso-

lution. The satisfying preliminary results demonstrate that the new DSFs are highly efficient in discriminating lesions from other candidate regions.

6. REFERENCES

- [1] N. Cheung, P. Mitchell, and T. Y. Wong, "Diabetic retinopathy." *Lancet*, vol. 376, pp. 124–36, Jul. 2010.
- [2] M. D. Abramoff, M. K. Garvin, and M. Sonka, "Retinal Imaging and Image Analysis," *IEEE Rev. Biomed. Eng.*, vol. 3, pp. 169–208, 2010.
- [3] M. Cree, J. Olson, K. McHardy, P. Sharp, and J. Forrester, "A Fully Automated Comparative Microaneurysm Digital Detection System," *Eye*, vol. 11, pp. 622–628, 1997.
- [4] M. Niemeijer, B. van Ginneken, J. Staal, M. Suttorp-Schulten, and M. D. Abramoff, "Automatic detection of red lesions in digital color fundus photographs." *IEEE Trans. Med. Imag.*, vol. 24, pp. 584–92, May 2005.
- [5] A. Fleming, S. Philip, K. Goatman, J. Olson, and P. Sharp, "Automated microaneurysm detection using local contrast normalization and local vessel detection." *IEEE Trans. Med. Imag.*, vol. 25, pp. 1223–32, Sep. 2006.
- [6] G. Quellec, M. Lamard, P. M. Josselin, G. Cazuguel, B. Cochener, and C. Roux, "Detection of lesions in retina photographs based on the wavelet transform." in *IEEE EMBS Conf.*, vol. 1, Jan. 2006, pp. 2618–21.
- [7] I. Lazar and A. Hajdu, "Retinal microaneurysm detection through local rotating cross-section profile analysis," *IEEE Trans. Med. Imag.*, vol. 32, pp. 400–7, Feb. 2013.
- [8] M. Niemeijer, B. van Ginneken, M. J. Cree, A. Mizutani, G. Quellec, C. I. Sanchez, B. Zhang, R. Hornero, M. Lamard, C. Muramatsu, X. Wu, G. Cazuguel, J. You, A. Mayo, Q. Li, Y. Hatanaka, B. Cochener, C. Roux, F. Karray, M. Garcia, H. Fujita, and M. D. Abramoff, "Retinopathy online challenge: automatic detection of microaneurysms in digital color fundus photographs." *IEEE Trans. Med. Imag.*, vol. 29, pp. 185–95, Jan. 2010.
- [9] R. Bernardes, P. Serranho, and C. Lobo, "Digital ocular fundus imaging: a review." *Ophthalmologica*, vol. 226, pp. 161–81, Jan. 2011.
- [10] L. Vincent, "Morphological grayscale reconstruction in image analysis: applications and efficient algorithms," *IEEE Trans. Image Process.*, vol. 2, pp. 176–201, Apr. 1993.
- [11] M. Grimaud, "A new measure of contrast: the dynamics," in *SPIE Image Alg. and Morpho. Image Process.*, vol. 1769, 1992, pp. 292–305.
- [12] L. Breiman, "Random Forests," *Mach. Learn.*, vol. 45, pp. 5–32, Oct. 2001.